Optics Letters

Higher-order topological states in two-dimensional Stampfli-Triangle photonic crystals

Yuchen Peng, Exian Liu, Bei Yan, Jianlan Xie, Aoqian Shi, Peng Peng, Hang Li, and Jianjun Liu*

Key Laboratory for Micro/Nano Optoelectronic Devices of Ministry of Education & Hunan Provincial Key Laboratory of Low-Dimensional Structural Physics and Devices, School of Physics and Electronics, Hunan University, Changsha 410082, China
**Corresponding author: jianjun.liu@hnu.edu.cn*

Received 28 February 2022; revised 20 May 2022; accepted 23 May 2022; posted 23 May 2022; published 7 June 2022

In this Letter, the higher-order topological state (HOTS) and its mechanism in two-dimensional Stampfli-Triangle (2D S-T) photonic crystals (PhCs) is explored. The topological corner states (TCSs) in 2D S-T PhCs are based on two physical mechanisms: one is caused by the photonic quantum spin Hall effect (PQSHE), and the other is caused by the topological interface state. While the former leads to the spin-direction locked effect which can change the distribution of the TCSs, the latter is conducive to the emergence of multiband TCSs in the same structure due to the characteristics of plentiful photonic bandgap (PBG) and broadband in 2D S-T PhCs. These findings allow new, to the best of our knowledge, insight into the HOTS, and are significant to the future design of photonic microcavities, high-quality factor lasers, and other related integrated multiband photonic devices.

https://doi.org/10.1364/OL.457058

For conventional topological insulators (TIs), d-dimensional TIs generally possess $(d-1)$-dimensional topological edge states (TESs) [1,2]. However, the higher-order TIs (HOTIs) exhibit the unconventional bulk-edge property that d-dimensional TIs possess gapless TESs lower than $(d-1)$-dimensions [3–7]. Among them, two-dimensional (2D) second-order TIs produce zero-dimensional gapless TESs, which are also called topological corner states (TCSs). The appearance of HOTIs provide new ideas for optical imaging [8] as well as photon localization [9] and optical waveguide transmission techniques [10–12]. Meanwhile, TCSs offer a simple method for the research of optical microcavities that does not require artificial structural defects [13], which is of great significance in the field of new-generation lasers [14] and other relative photonic devices [15].

When studying TCSs, attention is paid to the square lattice [8,9,16–20], kagome lattice [21–24], and honeycomb lattice [10,25–30] based on the 2D Su-Schrieffer-Heeger (SSH) model [31,32], or even extended to the quasicrystalline system [33,34]. Unlike the conventional lattices with translational symmetry, 2D photonic quasicrystals (PQCs) have the properties of rotational symmetry and long-range order. According to various works, PQCs combine the plentiful photonic bandgap (PBG) [35] and low refractive index threshold for producing a complete PBG [36], which make them advantageous over periodic photonic crystals (PhCs). However, calculating the band structure of PQCs is still a challenge. Therefore, the ability to form a PhC by periodizing the basic structural unit of the 2D PQC enables one to not only retain the advantages of the PQC, but also to obtain an accurate band structure for comprehensive research of the higher-order topological state (HOTS).

In particular, the two-dimensional Stampfli-Triangle (2D S-T) PhCs formed by a periodic arrangement of the triangular lattice composing the basic structural units of the Stampfli-type PQC satisfies C_6 symmetry and can realize the photonic quantum spin Hall effect (PQSHE) [37]. Compared to other structures with C_6 symmetry, the band structure of the 2D S-T PhCs is prone to broadening and enriching the PBG characteristics, which results in a greater PBG between the TES and the bulk state, providing a larger adjustment space for the generation of multiband TCSs. Meanwhile, the spin-direction locking effect in the PQSHE provides the possibility of spin-direction locked TCSs with variable distribution within the same structure.

Based on this, a simple method to obtain the TCS is proposed in this Letter. The technique consists of adjusting the diameters of the internal and external scatterers of the PhC to satisfy the time-reversal symmetry and achieve the exchangeable sequence of the bands. Then, combining it with PhCs that have no band order exchanged but share a common PBG, the spatial inversion symmetry at the interface between the two types of PhC is broken (the C_6 symmetry is broken into the C_3 symmetry). As a result, the gapped TESs are generated in their projected band, which can be regarded as an extension of the 2D SSH model. Moreover, TCSs based on two different physical mechanisms – one caused by the PQSHE and the other induced by the topological interface state – can be realized within the 2D S-T PhCs.

Examples of Stampfli-type PQCs and 2D S-T PhCs are shown in Fig. 1. The basic structural unit of a Stampfli-type PQC is an edge-to-edge splicing combination structure of an equilateral triangle and a square, which is rotated six times relative to a vertex of the triangle not involved into the combination as the rotation center. Therefore, it satisfies the C_6 symmetry, as shown in the blue grid in Fig. 1(a). The blue grid reduced to $1/\sigma = 0.268$ times according to the self-similarity factor $\sigma = 2 + 2\cos(2\pi/12)$ 3.732 of the Stampfli-type PQC can result in the lower right illustration. Therefore, the lattice structure of the Stampfli-type

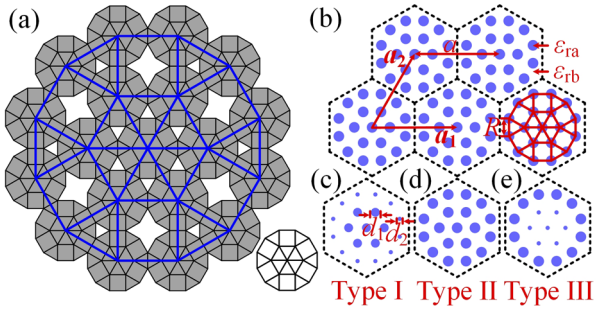

Fig. 1. Examples of Stampfli-type PQC and 2D S-T PhCs. (a) Stampfli-type PQC structure; (b) basic structural unit of a Stampfli-type PQC, arranged into a triangular lattice to form 2D S-T PhCs; (c) Type I: $d_2/d_1 < 1$; (d) Type II: $d_2/d_1 = 1$; (e) Type III: $d_2/d_1 > 1$.

PQC can be formed by taking the reduced basic structural unit as a lattice point placed at the blue grid. In turn, a 2D S-T PhC can be obtained using the basic structural units of the Stampfli-type PQCs arranged in a periodic triangular lattice (see Fig. 1(b)). Here, the lattice constant is set as $a = 1$ μm; the lattice basis vectors are $\boldsymbol{a}_1=(a, 0)$ and $\boldsymbol{a}_2=\left(a/2,\sqrt{3}a/2\right)$; the distance between the adjacent scatterers is $R=a/\left(3+\sqrt{3}\right)$ (which is also the lattice constant of the Stampfli-type PQC); and the diameters of the seven internal scatterers and twelve external scatterers are d_1 and d_2, respectively. Depending on the structural parameters, there are three basic structural units, as shown in Figs. 1(c)–1(e). Each basic structural unit is composed of germanium dielectric rods ($\varepsilon_{ra} = 16$) arranged in the air ($\varepsilon_{rb} = 1$).

It can be deduced that the Hamiltonian of the 2D S-T PhCs researched in this Letter satisfies the time-reversal symmetry, so that the sum of the total Berry curvature is zero (see Part I of Supplement 1for details). The 2D S-T PhCs also satisfy the C_6 rotation symmetry, the topological indices for the quanta of corner charge in terms of the band representations can be deduced from the rotation eigenvalues at the high symmetry points (HSPs) for all the bands below the PBG. The first-order and second-order topologically insulating phases are characterized by the bulk polarizations $\boldsymbol{P} = (P_x, P_y)$ and the fractional corner charge Q_c [19,38–40]. Under the condition of a zero Berry curvature, the bulk polarizations and secondary topological index are obtained, as follows:

$$P_x = P_y = [\mathrm{K}_1] + 2[\mathrm{K}_2] \bmod 1 \quad \textbf{(1)}$$

$$Q_c = \frac{1}{4}[\mathrm{M}_1] + \frac{1}{6}[\mathrm{K}_1] \bmod 1, \quad \textbf{(2)}$$

where $[\Pi_p] = \#\Pi_p - \#\Gamma_p$, and $\#\Pi_p$ is the number of occupied bands below the PBG at HSP Π with the rotation eigenvalue $\Pi_p = e^{2\pi i(p-1)/6}$ for $p = 1,2,3,\ldots,6$. Based on the theory of topological crystalline insulators, dipole moments are always vanishing for C_{6v} symmetric lattice due to $P_x = P_y = 0$ and if the fractional corner charge is $Q_c = 1/2$, a nontrivial second-order topological insulating phase is generated in 2D S-T PhCs. Details of the corresponding analysis of 2D S-T PhCs can be seen in Part II of Supplement 1.

The band structures of 2D S-T PhCs with different structural parameters were calculated, as shown in Fig. 2. It can be seen from Figs. 2(a)–2(c) that double Dirac points in the band structure undergo the evolution process from opening to degenerate and reopening when the 2D S-T PhC experiences a Type I-Type

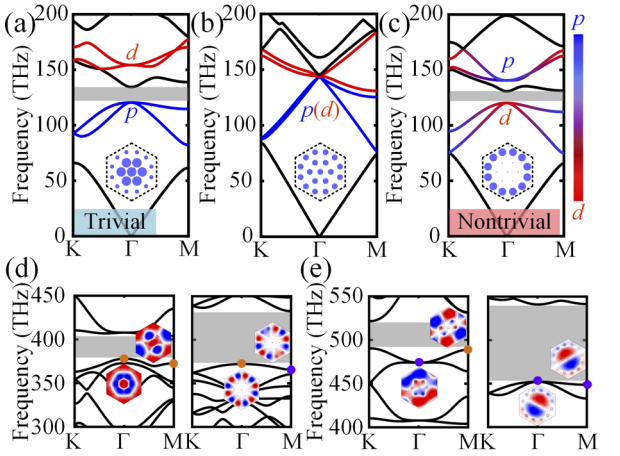

Fig. 2. Band structures of 2D S-T PhCs. (a) Type I: $d_1 = 0.9R$, $d_2 = 0.4R$; (b) Type II: $d_1 = d_2 = 0.6R$; (c) Type III: $d_1 = 0.1R$, $d_2 = 0.8R$. The band structures of Type I ($d_1 = 0.3R$, $d_2 = 0.1R$) and Type III ($d_1 = 0.1R$, $d_2 = 0.34R$) PhCs within different frequency bands (with a shared PBG but between the bands of different orders, namely the dislocated common PBG): (d) 300-450 THz; and (e) 400-550 THz. The illustration is the E_z field at the Γ and M points in the Brillouin zone, where the orange and purple dots represent even and odd parities, respectively.

II-Type III transformation. According to previous work in Ref. [37], the PQSHE can be realized in 2D S-T PhCs within the low frequency range, so the pseudospin degree of freedom is introduced [41]. However, for the high frequency range, compared to previous research in Ref. [26], although there is no regular *p*-*d* band inversion phenomenon within the low frequency band, there is still a breaking process at double Dirac points (see Part I of Supplement 1 for details). For Type I and Type III PhCs, the coupling coefficients between the scatterers are different due to their dissimilar diameters. Furthermore, there are bands with a topological nontrivial Zak phase, which lead to the appearance of TESs. These TESs are also called topological interface states [42,43]. When observing the parities at the Γ and M points in the Brillouin zone, they always have regular combination cases. In order to make the description more concise, the case where the Γ and M of the nearest neighboring band below the PBG with different parities is denoted as Nontrivial, and that with the same parities is denoted as Trivial [44]. Through numerous band calculations and rule summaries, it is found that as long as the band inversion occurs within the low frequency band, the Trivial (left) and Nontrivial (right) cases as shown in Fig. 2(d), and the Nontrivial (left) and Trivial (right) cases as shown in Fig. 2(e), appear below the dislocated common PBG of Type I and Type III PhCs within a high frequency range, as shown in Figs. 2(d) and 2(e). On the contrary, if there is no band inversion within the low frequency range, the same cases can also appear in two Type I or two Type III PhCs based on different materials (see Part III of Supplement 1 for details).

In order to further explore the topological characteristics of 2D S-T PhCs in different frequency bands as well as to verify the possibility of the emergence of gapped TESs, the projected band structures of the formed supercell were calculated, as shown in Fig. S3 of Supplement 1. For the low frequency band, the combined structure of Types I and III 2D S-T PhCs possesses a TES produced by the PQSHE. For the high frequency band, when Type I PhCs are combined with Type III PhCs without

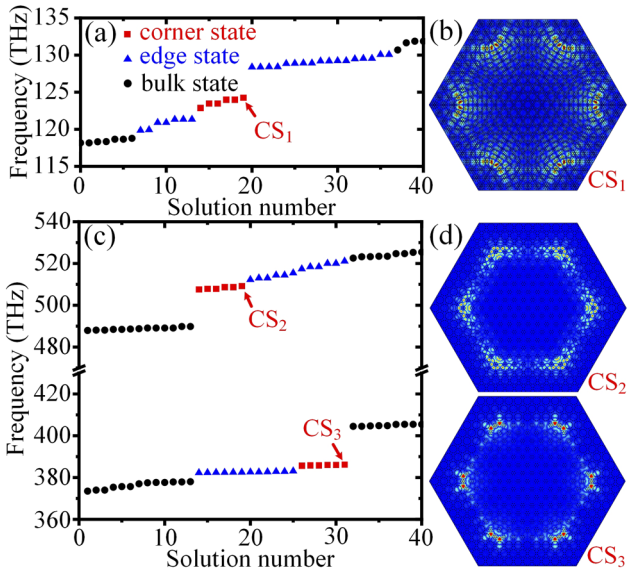

Fig. 3. (a) Eigenmodes solution number of the box-shaped structure as a combination of Type I ($d_1 = 0.9R$, $d_2 = 0.4R$) and Type III ($d_1 = 0.1R$, $d_2 = 0.8R$) 2D S-T PhCs; (b) field distribution of the corner state at 124.68 THz; (c) eigenmodes solution number of the box-shaped structure as a combination of Type I ($d_1 = 0.3R$, $d_2 = 0.1R$) and Type III ($d_1 = 0.1R$, $d_2 = 0.34R$) 2D S-T PhCs within the two frequency ranges; (d) field distribution of the corner state at 509.23 THz (upper panel) and 385.72 THz (lower panel).

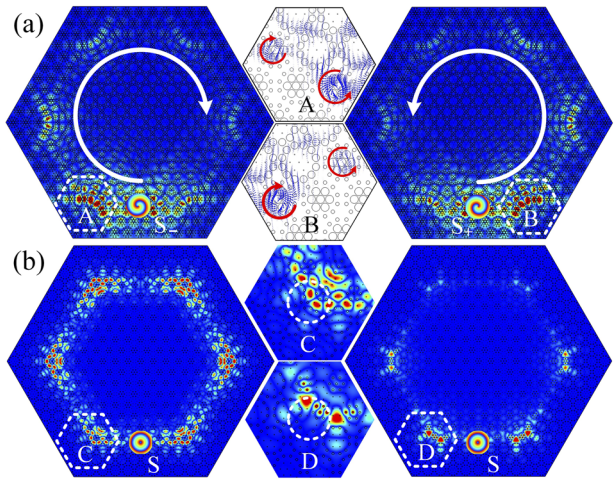

Fig. 4. (a) E_z field distribution after adding the light source $\mathbf{S}_{\pm} = H_0 e^{i\omega t}(\boldsymbol{e}_x \mp i\boldsymbol{e}_y)$ in the box-shaped waveguide without any defects (here, A and B denote time-averaged Poynting vector at corresponding area); (b) E_z field distribution after adding the line source in the box-shaped waveguide with different types of defects (here, C denotes impurities and D denotes cavity).

band inversion but share a dislocated common PBG, a gapped TES will be generated due to different combinations of parities below the PBG between the two PhCs (see Part III of Supplement 1 for details). In addition, two Type I or two Type III PhCs are found to produce TESs in the projected bands as long as their nearest neighboring bands below the dislocated common PBG are the specific combinations of Nontrivial and Trivial cases generated (see Part IV of Supplement 1 for details). Therefore, it is possible for 2D S-T PhCs to realize TCSs based on different physical mechanisms.

In order to elucidate whether TCSs can be generated, it is necessary to design a box-shaped structure and solve its eigenmodes, as shown in Fig. 3. The blue triangles and black dots in Figs. 3(a) and 3(c) corresponding to the TESs and the bulk states, respectively, cover the same frequency range as that in Fig. S3 of Supplement 1. However, there are the independent solutions (represented by the red rectangles) in the PBG, which do not belong to the projected band structures from Fig. S3 of Supplement 1. In this respect, the eigenmode field distribution corresponding to three representative points is later analyzed, as shown in Figs. 3(b) and 3(d). In the obtained graphs, the electric fields are all concentrated at the six corners inside the box-shaped structure, which proves the feasibility of realizing TCSs by considering only the combination of parities of the nearest neighboring band below the dislocated common PBG.

The waveguide is constructed via simulation to further verify whether TCSs can be produced in reality and defects can be overcome. The TCS generated by the TES of the PQSHE has a spin-direction locked relationship, as shown in Fig. 4(a). Similar to the generation of the TES, TCSs with decreasing strength in a counterclockwise or clockwise direction can also be excited by using light sources with different circular polarization directions. The time-averaged Poynting vectors show that the light concentrates around the basic structural unit with different directions of rotation, which further demonstrates the TCS is generated by PQSHE. Meanwhile, the reason why strength decreases gradually can also be explained by the time-averaged Poynting vectors. As shown in the inset of Fig. 4(a), the flow of energy shows the same performance as the slow light effect [45], which means there is a less effective coupling path far away from the source in the box-shaped structure. Therefore, a TCS with decreasing strength in a counterclockwise or clockwise direction can be realized. For the TCS generated by the topological interface state, two different defects are introduced according to the graph in Fig. 4(b). Here, the electric fields are still located at six corners, being immune to the surrounding defects (see Part VI of Supplement 1 for details about the schematics of the defects) and demonstrating their protection by the topology. Moreover, the TCS in a parallelogram box-shaped structure is also analyzed to show the versatility and stability of the proposed method (see Part VII of Supplement 1 for details). Meanwhile, in order to verify the realization of the TCS for the optical frequency, we have constructed the half-hexagonal box-shaped structure and numerically verified the emergence of the TCS within low frequency when considering the metal substrate (see Part VIII of Supplement 1 for details), which can provide an experimental scheme for realizing TCSs in 2D S-T PhCs.

In this Letter, the diameters of the scatterers of the 2D S-T PhCs were changed to generate three different types of basic structural units: larger internal scatterers with smaller external scatterers; those with consistent outer and internal diameters; and smaller internal with larger external scatterers. Due to the broken C_6 symmetry at the interface, the order of bands could be exchanged, resulting in topological phase transition. Moreover, besides the band inversion of the two PhCs, there was also the opening, degenerate and reopening of double Dirac points in the dislocated common PBG within other frequency bands. The combined supercell structure of the two PhCs was calculated

to obtain the gapped TES. Compared to other structures with C_6 symmetry, 2D S-T PhCs were shown to be more likely to generate a broad and plentiful PBG. Moreover, as long as the nearest neighboring bands below the dislocated PBG possessed different combinations of parities, a gapped TES and TCS could be generated. Thus, a simple method was developed to realize TCSs, which also opened up new prospects for the implementation of multiband TCSs. Finally, a waveguide was constructed and different sources along with defects were added to confirm the emergence of TCSs with different physical mechanisms and to verify their topological protection.

Funding. Fundamental Research Funds for the Central Universities (531118040112); Natural Science Foundation of Hunan Province (2017JJ2048, 2020JJ4161); National Natural Science Foundation of China (61405058, 62075059).

Acknowledgment. The authors acknowledge Professor Jian-Qiang Liu for software sponsorship.

Disclosures. The authors declare no conflicts of interest.

Data availability. Data underlying the results presented in this Letter are not publicly available at this time but may be obtained from the authors upon reasonable request.

Supplemental document. See Supplement 1 for supporting content.

REFERENCES

1. M. Z. Hasan and C. L. Kane, Rev. Mod. Phys. **82**, 3045 (2010).
2. X. L. Qi and S. C. Zhang, Rev. Mod. Phys. **83**, 1057 (2011).
3. W. A. Benalcazar, B. A. Bernevig, and T. L. Hughes, Science **357**, 61 (2017).
4. W. A. Benalcazar, B. A. Bernevig, and T. L. Hughes, Phys. Rev. B **96**, 245115 (2017).
5. M. Kim, Z. Jacob, and J. Rho, Light: Sci. Appl. **9**, 130 (2020).
6. B. Xie, H.-X. Wang, X. Zhang, P. Zhan, J.-H. Jiang, M. Lu, and Y. Chen, Nat. Rev. Phys. **3**, 520 (2021).
7. D. V. Zhirihin and Y. S. Kivshar, Small Science **1**, 2100065 (2021).
8. Z. Zhang, H. Long, C. Liu, C. Shao, Y. Cheng, X. Liu, and J. Christensen, Adv. Mater. **31**, 1904682 (2019).
9. Y. Ota, F. Liu, R. Katsumi, K. Watanabe, K. Wakabayashi, Y. Arakawa, and S. Iwamoto, Optica **6**, 786 (2019).
10. Y. Yang, Z. Jia, Y. Wu, R.-C. Xiao, Z. H. Hang, H. Jiang, and X. C. Xie, Sci. Bull. **65**, 531 (2020).
11. A. Shi, B. Yan, R. Ge, J. Xie, Y. Peng, H. Li, W. E. I. Sha, and J. Liu, Opt. Lett. **46**, 1089 (2021).
12. X.-T. He, M.-Y. Li, H.-Y. Qiu, W.-S. Ruan, L.-D. Zhou, L. Liu, X.-D. Chen, W.-J. Chen, F.-L. Zhao, and J.-W. Dong, Photonics Res. **9**, 1423 (2021).
13. X. Xie, W. Zhang, X. He, S. Wu, J. Dang, K. Peng, F. Song, L. Yang, H. Ni, Z. Niu, C. Wang, K. Jin, X. Zhang, and X. Xu, Laser Photonics Rev. **14**, 1900425 (2020).
14. W. Zhang, X. Xie, H. Hao, J. Dang, S. Xiao, S. Shi, H. Ni, Z. Niu, C. Wang, K. Jin, X. Zhang, and X. Xu, Light: Sci. Appl. **9**, 109 (2020).
15. H. Li, R. Ge, Y. Peng, B. Yan, J. Xie, J. Liu, and S. Wen, Sci. China-Phys. Mech. Astron. **64**, 124211 (2021).
16. B. Y. Xie, H. F. Wang, H. X. Wang, X. Y. Zhu, J. H. Jiang, M. H. Lu, and Y. F. Chen, Phys. Rev. B **98**, 205147 (2018).
17. C. W. Peterson, W. A. Benalcazar, T. L. Hughes, and G. Bahl, Nature **555**, 346 (2018).
18. X.-D. Chen, W.-M. Deng, F.-L. Shi, F.-L. Zhao, M. Chen, and J.-W. Dong, Phys. Rev. Lett. **122**, 233902 (2019).
19. B. Y. Xie, G. X. Su, H. F. Wang, H. Su, X. P. Shen, P. Zhan, M. H. Lu, Z. L. Wang, and Y. F. Chen, Phys. Rev. Lett. **122**, 233903 (2019).
20. J. Jiang, B. Yan, Y. Peng, J. Xie, A. Shi, and J. Liu, Opt. Lett. **47**, 437 (2022).
21. H. Xue, Y. Yang, F. Gao, Y. Chong, and B. Zhang, Nat. Mater. **18**, 108 (2019).
22. A. El Hassan, F. K. Kunst, A. Moritz, G. Andler, E. J. Bergholtz, and M. Bourennane, Nat. Photonics **13**, 697 (2019).
23. M. Li, D. Zhirihin, M. Gorlach, X. Ni, D. Filonov, A. Slobozhanyuk, A. Alù, and A. B. Khanikaev, Nat. Photonics **14**, 89 (2020).
24. A. Vakulenko, S. Kiriushechkina, M. Wang, M. Li, D. Zhirihin, X. Ni, S. Guddala, D. Korobkin, A. Alù, and A. B. Khanikaev, Adv. Mater. **33**, 2004376 (2021).
25. H. Fan, B. Xia, L. Tong, S. Zheng, and D. Yu, Phys. Rev. Lett. **122**, 204301 (2019).
26. Z. Zhang, B. Hu, F. Liu, Y. Cheng, X. Liu, and J. Christensen, Phys. Rev. B **101**, 220102 (2020).
27. B. Xie, G. Su, H.-F. Wang, F. Liu, L. Hu, S.-Y. Yu, P. Zhan, M.-H. Lu, Z. Wang, and Y.-F. Chen, Nat. Commun. **11**, 3768 (2020).
28. M. Jung, R. Gladstone, and G. Shvets, Adv. Photonics **2**, 046003 (2020).
29. S. Wu, B. Jiang, Y. Liu, and J.-H. Jiang, Photonics Res. **9**, 668 (2021).
30. Y. Wei, B. Yan, Y. Peng, A. Shi, D. Zhao, R. Peng, Y. Xiang, and J. Liu, Opt. Lett. **46**, 3941 (2021).
31. W. P. Su, J. R. Schrieffer, and A. J. Heeger, Phys. Rev. Lett. **42**, 1698 (1979).
32. F. Liu and K. Wakabayashi, Phys. Rev. Lett. **118**, 076803 (2017).
33. R. Chen, C.-Z. Chen, J.-H. Gao, B. Zhou, and D.-H. Xu, Phys. Rev. Lett. **124**, 036803 (2020).
34. C.-B. Hua, R. Chen, B. Zhou, and D.-H. Xu, Phys. Rev. B **102**, 241102 (2020).
35. Y. S. Chan, C. T. Chan, and Z. Y. Liu, Phys. Rev. Lett. **80**, 956 (1998).
36. M. E. Zoorob, M. D. B. Charlton, G. J. Parker, J. J. Baumberg, and M. C. Netti, Nature **404**, 740 (2000).
37. B. Yan, J. L. Xie, E. X. Liu, Y. C. Peng, R. Ge, J. J. Liu, and S. C. Wen, Phys. Rev. Appl. **12**, 044004 (2019).
38. M. Ezawa, Phys. Rev. Lett. **120**, 026801 (2018).
39. W. A. Benalcazar, T. Li, and T. L. Hughes, Phys. Rev. B **99**, 245151 (2019).
40. Y. Liu, S. Leung, F.-F. Li, Z.-K. Lin, X. Tao, Y. Poo, and J.-H. Jiang, Nature **589**, 381 (2021).
41. M. Xiao, Z. Q. Zhang, and C. T. Chan, Phys. Rev. X **4**, 021017 (2014).
42. X. Huang, Y. Yang, Z. H. Hang, Z.-Q. Zhang, and C. T. Chan, Phys. Rev. B **93**, 085415 (2016).
43. C. Guan, J. Shi, J. Liu, H. Liu, P. Li, W. Ye, and S. Zhang, Laser Photonics Rev. **13**, 1800242 (2019).
44. F. Liu, H. Y. Deng, and K. Wakabayashi, Phys. Rev. B **97**, 035442 (2018).
45. Y. Peng, B. Yan, J. Xie, E. Liu, H. Li, R. Ge, F. Gao, and J. Liu, Phys. Status Solidi RRL **14**, 2000202 (2020).